Catalysis Science & Technology

Accepted Manuscript

ROYAL SOCIETY OF CHEMISTRY

www.rsc.org/catalysis

Catalysis Science & Technology RSCPublishing

ARTICLE

Tailoring the Physicochemical Properties of Zeolite Catalysts

Cite this: DOI: 10.1039/xoxxoooooox

J.D. Rimer,[a*] M. Kumar,[a] R. Li,[a] A.I. Lupulescu,[a] and M.D. Oleksiak[a]

Received ooth January 2012,
Accepted ooth January 2012

DOI: 10.1039/xoxxoooooox

www.rsc.org/

The physicochemical properties of zeolite catalysts, such as crystal topology, composition, size, and morphology, can have a marked effect on their performance for a broad range of reactions – notably catalyst activity, hydrothermal stability, shape selectivity, and/or lifetime. There are relatively few zeolite framework types employed as commercial catalysts. Contributing factors include the high cost of synthesis and the difficulty of tailoring crystal nucleation and growth to achieve the desired properties. There is an increasing amount of structure-performance data in literature and patents that can be used to guide the identification of effective zeolite "formulations"; however, the challenges for realizing these materials are generally twofold: (i) growth mechanisms are not well understood, which often prohibits the control of zeolite crystallization; (ii) the impracticality of most design schemes hinder their economic feasibility and their potential for facile implementation. These aspects are often overlooked in the design of zeolite catalysts, yet they are essential for any plans aimed at eventual commercialization. In this review we summarize our recent findings in the area of zeolite synthesis and characterization, focusing specifically on practical routes to control zeolite crystallization in the absence of costly organics, tailoring crystal habit through the use of versatile and recyclable zeolite growth modifiers, and pioneering techniques in zeolite surface science as a platform to expand our knowledge of crystal growth mechanisms. These concerted efforts in rational design bridge fundamental and applied research towards the development of zeolites with improved catalytic performance.

Introduction

Zeolites are utilized as heterogeneous catalysts in petroleum refining and chemicals production, and have also proven to be active catalysts in areas of biofuels[1], emissions (e.g., selective catalytic reduction, SCR[2-4]), and C_1 chemistry (e.g., methanol-to-hydrocarbons, MTH[5, 6], and oxidative coupling of methane, OCM[7]). Challenges confronting zeolite design are similar to those encountered in the synthesis of most catalysts, which are the need to develop efficient approaches to improve catalyst activity, selectivity, and lifetime through facile, versatile, and inexpensive routes.

The unique physicochemical properties of zeolites include their tunable acidity and shape selectivity. The latter is largely determined by the crystal structure, which is comprised of periodically-ordered channels and/or cages of varying size and dimensionality. While more than 200 zeolite framework types have been synthetically realized[8], it is interesting to note that fewer than 10 are used in industrial processes. One reason for the relatively small number of commercial zeolites is the high cost of preparation, which is primarily attributed to the use of organic structure-directing agents (OSDAs), which are molecules with sizes and shapes that are commensurate with zeolite channels or cages and help facilitate their formation. The vast majority of zeolite frameworks can only be synthesized with OSDAs, yet their expense and the inability to recycle OSDAs due to post-synthesis calcination required to remove occluded molecules is cost-prohibitive and hinders their broader utility in commercial applications. Beyond their capability for tuning crystal topology, additional advantages of OSDAs include their ability to alter the silicon-to-aluminum ratio (SAR) of zeolites[9, 10], which affects catalyst acidity (i.e., Brönsted acid sites). Conversely, OSDA-free syntheses most often produce low SAR materials, which are susceptible to rapid deactivation (e.g., coking) and exhibit lower hydrothermal stability.

Zeolite crystal topology and acidity are critical parameters that influence catalyst performance. Two physical properties that also play important roles are crystal size and morphology. Prior studies have shown that crystal habit can alter reaction conversion and product selectivity, but has a more significant impact on catalyst lifetime[11, 12]. Zeolites have a tendency to naturally form sub-optimal (poorly engineered) crystals where the pore channels are oriented along the longest crystal dimension(s), which generates long internal diffusion path length for sorbates. Moreover, zeolite crystals tend to present pore openings on small exterior surface area, which restricts sorbate access to active sites within the zeolite. Longer diffusion path length increases the propensity of coke formation within the channels and cages, thereby inciting rapid catalyst deactivation. Recent examples of catalyst design have shown that crystal habit can significantly improve catalyst lifetime. For instance, Ryoo and coworkers [13] prepared ultrathin ZSM-5

crystals (MFI type) with dimensions of several unit cell lengths (ca. 2 nm) and demonstrated a four-fold increase the time-on-stream activity in MTH compared to commercial ZSM-5. Indeed, the ability to control zeolite crystallization and tailor their physical properties offers significant potential for reducing the rate of coking, which is critical for MTH, biofuels, and many other catalytic processes.

A common method of controlling zeolite crystallization is altering synthesis parameters[14-17] which include (but are not limited to) temperature, water content, and the molar composition of SiO_2 and Al_2O_3. This approach is marginally effective for a select number of zeolite structures. Alternative techniques include the use of OSDAs, which accounts for the success that Ryoo and others[18, 19] have had in the generation of ultrathin (or hierarchical) zeolites. Delamination (or exfoliation) procedures can produce crystalline sheets with unit cell dimension [20-22], while nano-sized crystallites can be prepared with the use of templates (e.g., carbon templates [19, 23, 24]), polymeric additives [25, 26], or colloidal stabilizers (e.g., surfactants [27-29]). We recently showed that zeolite size and morphology can be selectively tailored using zeolite growth modifiers (ZGMs) [30, 31], which are inexpensive and commercially-available organics that can be recovered and recycled. To this end, ZGMs offer a facile, versatile, and economic approach to predictively tune crystal habit.

Herein we highlight recent work in our group that addresses three elements of zeolite catalyst design: (i) Expanding the use of OSDA-free synthesis to broaden the list of commercial zeolite catalysts, (ii) investigating the efficacy and mode of action of ZGMs to tailor crystal size and shape, and (iii) developing techniques that enable fundamental studies of growth mechanisms *in situ*. Collectively, this work focuses on commercially viable methodologies for the predictive control of zeolite growth in order to achieve catalysts with desirable physiochemical properties that display optimal performance in a wide range of catalytic reactions.

Discussion

The "Art" of OSDA-Free Synthesis

The limited number of commercial zeolites prepared without OSDAs include common catalysts such as ZSM-5, faujasite (FAU type, or X/Y), and mordenite (MOR type). To date there are only 32 zeolites (i.e., <15 % of known structures)[32] that have been prepared synthetically by OSDA-free methods, while over 57 structures have been identified as natural minerals [33]. Despite the significant research effort focused on controlling zeolite crystallization, OSDA-free synthesis remains more of an art than a science. This is partly attributed to the diversity of growth compositions (e.g., gels, solutions, and solids) that are complex in nature. Moreover, zeolite preparation is complicated by the fact that subtle modifications in synthesis conditions can impart dramatic changes in the crystal product – the mechanistic explanations for which are not fully reconciled.

The open framework structures of zeolites have similar free energies of formation [34], which can explain why it is often difficult to control crystallization. It also stresses the importance of kinetics, i.e., the need for OSDAs to facilitate the formation of a desired crystal phase. Along these lines, zeolites are thermodynamically metastable relative to more dense silicates, such as quartz, which engenders the frequent formation of crystal polymorphs (i.e., impurities). A common phenomenon observed in zeolite synthesis is the Ostwald rule of stages, which is an empirical rule observed in many systems wherein the initial structure that forms is metastable, but with increased time and/or temperature undergoes a series of structural transformations to more thermodynamically stable crystals.[35] The relative role of thermodynamics and kinetics in these transformations is not well understood, at least to the extent that it is possible to predict the formation of crystal phase(s). As such, selecting an appropriate set of synthesis parameters to achieve a desired phase is often convoluted.

Zeolites that form via OSDA-free routes are usually restricted in their SAR. Examples include structures with double-6-membered ring (d6R) secondary building units, such as FAU and zeolite L (LTL type), which are limited to SAR < 4 (presumably due to the unfavourable energetics of Si substitution in the d6R) [36]. In some instances, zeolites have a propensity to crystallize with SAR ≈ 1, such as zeolite A (LTA type). In many cases, siliceous zeolites can be synthesized only through the use of OSDAs[10] and/or fluoride growth media[37, 38]. This is one of the most significant challenges for extending the list of commercial zeolite catalysts prepared in the absence of OSDAs. Zeolite A is an exemplary case study since its nominally high Al content is prohibitive for catalytic reactions,

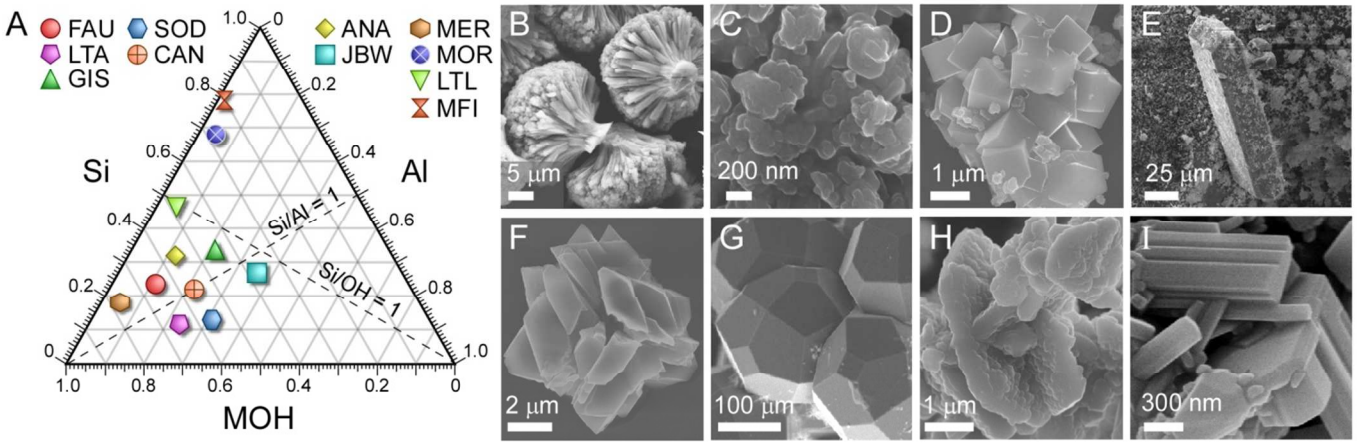

Figure 1. (A) Kinetic phase diagram highlighting representative molar fractions of zeolites prepared with alkali metals ($M^+ = Na^+$ or K^+) and without OSDAs (Table S1 in SI lists specific growth conditions). Scanning electron micrographs of the zeolite crystals (B) K-MER, (C) Na-FAU, (D) Na-LTA, (E) Na-JBW, (F) Na-GIS, (G) Na-ANA, (H) Na-SOD, and (I) Na-CAN. Images of K-LTL and Na-MOR are in Figures 2 and 3.

Catalysis Science & Technology RSCPublishing

ARTICLE

yet studies have shown that increased silica content (SAR = 3) produces an active catalyst for hydrogenation of olefins with improved hydrothermal stability.[39] Generating Si-rich materials in the absence of OSDAs is a desirable, albeit challenging goal in zeolite synthesis. An alternative approach is to reduce, but not completely eliminate, the organic. One promising example is seeded growth where crystals prepared with OSDAs can be used as seeds (after calcination) in OSDA-free growth solutions [40-42]. Examples include the use of BEA seeds to prepare BEA [43, 44], ZSM-22 (TON) seeds to prepare TON [45], and ZSM-23 (MTT) seeds to prepare MTT crystals [46]. Alternatively, seeds prepared by OSDA-free routes can be used, such as the use of LTL seeds to prepare ZSM-34, which is an intergrowth of erionite (ERI) and offretite (OFF) [47, 48].

An interesting observation in zeolite synthesis is the dramatic difference in crystal size and morphology that occurs despite inherent similarities in synthesis compositions (see Figure 1). Indeed, small changes in the molar ratio of key components (i.e., Si, Al, and OH^-), temperature, and/or the time of hydrothermal treatment yields substantial differences in the crystal structure (Figure 1A) and habit (Figure 1, B - I). Scanning electron micrographs of different framework types reveal a large variation in crystal dimensions spanning ca. 50 nm to 100 μm. The crystal morphology is also diverse, ranging from spheroidal particles with indistinct habit (e.g., Na-FAU and Na-SOD), to polycrystalline aggregates (e.g., K-MER and Na-GIS), to well-defined shapes such as cubes (e.g., Na-LTA), cylinders or rods (e.g., K-LTL and Na-CAN), and polyhedrons (e.g., Na-ANA and Na-JBW).

The selection of alkali metals in growth solutions is critical since extraframework cations often serve as inorganic structure-directing agents. A recent example by Maartens and coworkers showed that hydrothermal treatment of FAU in the presence of alkali hydroxides, using Li^+, K^+, Cs^+, and Rb^+, resulted in a structural transformation to low silicon ABW, CHA, ANA, and MER frameworks, respectively [49]. We have shown that kinetic (ternary) phase diagrams are a useful way of mapping the parameter space for synthesizing pure crystal phases [35]. Ternary diagrams are constructed with the molar fractions of Si, Al, and MOH (where M^+ = alkali metal) while keeping all other parameters fixed. The diagram in Figure 1A is a superposition of multiple phase diagrams compiled from syntheses at various temperature, time, and compositions (for more details see Table S1 in the Supplementary Information, SI). These diagrams serve as a platform for tuning zeolite phase purity as well as exploring conditions that lead to more Si-rich structures.

Chabazite (CHA type) is an example of a zeolite that can be synthesized by OSDA-free routes, but requires the organic to achieve sufficiently high SAR for catalysis. The unique shape selectivity and excellent hydrothermal stability of CHA has led to its use in SCR and MTH reactions, and has motivated efforts to identify structural analogues (i.e., 8-MR zeolites [50]) with potentially superior performance. As previously noted, CHA crystals prepared in the absence of an OSDA are limited to SAR < 3. Similar compositional restrictions are encountered when preparing 8-MR zeolites such as LTA, GIS, and ANA. It

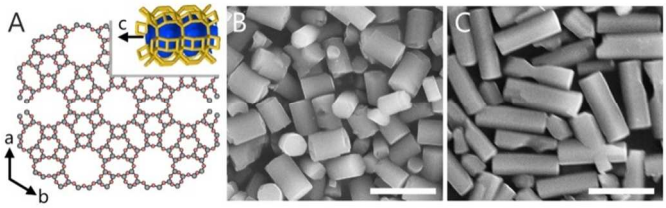

Figure 2. LTL crystallization. (A) LTL is a hexagonal structure with a P6/mmm space group (a = 1.81, b = 1.81, c = 0.76 nm; α = β = 90°, γ = 120°; $\underline{V}$ = 36.0 cm^3/mol). (B) Scanning electron micrographs of K-LTL prepared at a molar ratio 10 KOH:z H_2O (z = 505). LTL crystallization is sensitive to water content. (C) SEM image of crystals prepared with increased water content, z = 603. Scale bars equal 5 μm.

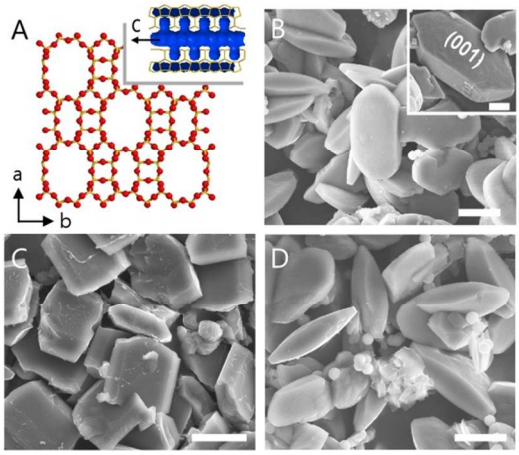

Figure 3. MOR crystallization. (A) MOR is an orthorhombic structure with a Cmcm space group (a = 1.83, b = 2.05, c = 0.75 nm; α = β = γ = 90°; $\underline{V}$ = 35.4 cm^3/mol). (B) Na-MOR crystals are hexagonal platelets with (001) basal faces (inset). Scanning electron micrographs of crystals synthesized in the presence of (C) cyclohexane-1,4-diol and (D) tributylphosphine oxide (TBPO). These ZGMs result in an elongation of crystal dimension in the c-direction and a narrowing of the (001) surface area, respectively. Scale bars equal 10 μm.

has been reported that the incorporation of metals within these structures produces active catalysts. For instance, Iglesia and Zones [51] showed that noble metals can be incorporated into 8-MR zeolites using a *ship in a bottle* like approach that places ligand stabilized metals in metastable zeolites with larger pores that are then transformed into more thermodynamically stable structures (e.g., GIS or ANA) with smaller pores. This permits the occlusion of metals in zeolite cages that otherwise would be challenging to accomplish via post-synthesis ion exchange due to the restricted diffusion of hydrated ions through pores with small aperture. Using low SAR zeolites as acid catalysts, however, is difficult since the calcination temperature required to activate the catalyst (generating H-zeolites) can often result in a loss of crystallinity.

Here we highlight two zeolite catalysts prepared by OSDA-free methods, LTL and MOR, to illustrate the ability (and complexity) of tailoring crystal size and habit by changing

synthesis parameters. Both of these zeolites possess 1D, 12-MR pores (Figures 2A and 3A). Moreover, both crystals are prepared with similar synthesis conditions (Table S1). Nominally LTL forms cylindrical crystals (Figure 2B) with a length-to-diameter aspect ratio of ca. 2. LTL crystal shape is sensitive to changes in synthesis parameters[52-54]. For instance, decreasing the temperature from 180 to 100 °C reduces the aspect ratio by a factor of 4, producing thin cylindrical disks with dramatically shorter diffusion path length along c-oriented channels [30]. An increase in water content has the opposite effect, producing high aspect ratio cylinders, as shown in Figure 2C.[30] Similar effects have been reported for MOR, which most commonly exhibit hexagonal platelet morphology (Figure 3B). Changes in synthesis parameters, such as the molar ratios SiO_2/H_2O, SiO_2/Al_2O_3, and $NaOH/SiO_2$, increase the thickness of MOR platelets along the c-direction [55], generating high aspect ratio rods; however, unlike LTL, attempts to reduce the aspect ratio of MOR crystals to generate thin platelets with shorter 1D channels has been unsuccessful. Indeed, it is well known that preparing MOR crystals with sizes less than 1 μm is a challenging task [56], while LTL can be readily synthesized with dimensions as low as 60 nm through OSDA-free methods.[57] This dichotomy is interesting given the similarity of LTL and MOR pore structure and unit cell parameters. A limited understanding of the factors governing zeolite crystallization is a major hindrance for efforts aimed at transitioning zeolite synthesis from that of an art to a science.

Discovering Efficient Methods for Rational Design

The term "rational design" is often used without definition. Here we invoke B. Fuller's description of a designer that encompasses the multifaceted nature of rational design: "A designer is an emerging synthesis of artist, inventor, mechanic, objective economist, and evolutionary strategist." Many of the ideas proposed in zeolite synthesis to tailor the physicochemical properties of catalysts fail to consider the economics of the approach, as well as its ease of use and its versatility for a broad class of materials. The most cost-prohibitive aspect of zeolite synthesis is the use of OSDAs. For zeolites like CHA that are active catalysts in multiple high-impact applications, the cost of producing the organic can be reduced on the basis of the economy of scales [58]; however, this opportunity is only afforded to a small subset of zeolite structures. Indeed, substantial progress to expand the list of commercial zeolites will likely require the use of OSDAs. As such, it is advantageous to find ways of optimizing catalyst performance to partially offset the costs of OSDA usage. For instance, more expensive catalysts can be justified if their lifetime is enhanced – an outcome that can be accomplished by reducing the rate of deactivation (e.g., coking), either by adjusting SAR to more Si-rich materials or tuning catalyst size and shape through crystal engineering. Here we address the latter by providing an overview of ZGMs, which are a facile, versatile approach to tailor zeolite crystallization.

Growth modifiers are common in nature, often functioning as regulators of biogenic crystals or operating as inhibitors of pathological diseases. Modifiers are also employed in synthetic processes to tailor the habit (and in some instances the polymorph) of inorganic and organic crystals. The types of modifiers encountered in literature range from ions and small molecules to macromolecules (e.g., proteins and polymers). The mechanism of growth modification is a kinetic effect that is often described in relation to classical modes of crystal growth

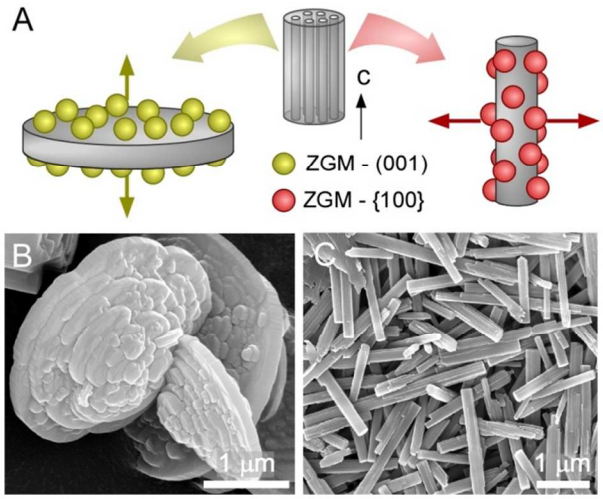

Figure 4. Effects of growth modifiers on LTL crystal habit. (A) Illustration of modifier-crystal interactions on the (001) and {100} surfaces, producing (B) low aspect ratio discs and (C) high aspect ratio rod-like crystals, respectively. LTL crystals in the SEM images were prepared with the following modifiers: (B) 1,2,3-hexanetriol (10 wt%) and (C) PDDAC (2 wt%).

(i.e., layer-by-layer mechanisms; see Figure 6)[59]. Modifiers that possess site specificity for a crystallographic face bind to the surface and impede crystal growth by two possible routes: (i) adsorption on terraces to reduce 2D layer nucleation and induce step pinning; and/or (ii) binding to steps to impede solute attachment to kink sites. Each mechanism effectively reduces the velocity of step advancement, thereby reducing the rate of crystallization.

The impact of ZGMs has been demonstrated for two zeolite framework types: LTL and MFI. A systematic investigation of alcohols and amines revealed heuristic guidelines for tuning modifier site specificity and efficacy. In the case of LTL synthesis, our studies revealed that alcohols are inhibitors of growth along the axial c-direction (Figure 4, A and B), which reduces the length-to-diameter aspect ratio of the cylinders, resulting in ultrathin discs with less than 100 nm in thickness [30]. These studies revealed that the most effective alcohols had a minimum of three sequential carbons in the backbone, $(CH_2)_3$. Moreover, the spatial positioning of alcohols on the first and third carbon was more effective than other combinations tested for a range of diols and triols, which suggests the spatial confirmation of binder moieties facilitates hydrogen binding between alcohols on the modifier and the terminal ≡SiOH or ≡AlOH groups presented on the LTL (001) surface. We also observed that an increase in hydrophobicity enhanced modifier efficacy up to a certain ZGM carbon backbone length, beyond which there was little added effect of increasing the hydrophobicity. One aspect that was not addressed in our previous study is the impact of chirality. The chiral molecules selected as modifiers were racemic; therefore, it is uncertain if one of the enantiomers is more effective than the other. We are currently working on molecular modelling to elucidate the binding modes of ZGMs on zeolite surfaces.

Prior studies have shown that positively-charged modifiers, such as PDDAC (polydiallyldimethylammonium chloride), preferentially interact with LTL [30] surfaces, resulting in the formation of high aspect ratio rod-like crystals (Figure 4, A and C)[30]. An additional observation was the relatively high efficacy of polymers compared to smaller molecules (e.g., constitutive monomers). The proximal binding groups on macromolecules

facilitate their strong adsorption on crystal surfaces. ZGM site specificity arises from molecules residing on a particular crystal surface for a longer time (on average) than other surfaces. This delays solute flux to the surface, thereby altering the rate of anisotropic growth with a concomitant change in bulk crystal habit. Polymers are promising modifiers on the basis of their high potency, which minimizes the necessary quantity of ZGM (e.g., < 0.2 wt% PDDAC is effective). Moreover, ZGMs can be recovered by simply washing the zeolite with water, which opens the possibility for recycling. Additional advantages of this facile approach are the low cost of commercially available molecules, and the potential ease of integrating modifiers into the existing infrastructure of commercial crystallization.

The versatility of modifiers has proven to be effective for tailoring a wide range of catalysts, including metals and metal oxides[60-62]. One challenge of using this technique is the uncertainty of selecting an appropriate ZGM *a priori* without knowledge of modifier-crystal molecular recognition. For instance, we found that a majority of the ZGMs that were effective modifiers of LTL crystallization had little effect on MOR crystallization. A list of the molecules screened as putative modifiers of MOR are presented in Table S2 of the SI. We did observe two molecules that influenced MOR habit, although not to the desired effect of reducing [001] dimensions. Instead, we identified molecules that bind to the sides of MOR platelets. For example, cyclohexane-1,4-diol appears to bind to the faces presented on all sides to generate high aspect ratio rod-like crystals (Figure 3C). The molecule tributylphosphine oxide (TBPO) exhibits greater site specificity for the sides of MOR crystals, resulting in the formation of elongated hexagonal platelets (Figure 3D).

It is reasonable to expect that LTL and MOR, on the basis of their similar structures, would share a common set of ZGMs; however, the modifiers identified for MOR had no apparent effect on LTL crystallization. Conversely, we have observed cases where a ZGM is effective for more than one zeolite type. For instance, we tested the most effective modifiers of LTL in silicalite-1 (MFI type) synthesis and observed changes in crystal habit, but the impact on MFI was marginal compared to that of LTL. Likewise, the most effective ZGMs for MFI had markedly less impact on LTL. Collectively, these observations emphasize the unique nature of modifier-crystal interactions.

Investigations of silicalite-1 synthesis revealed that amines had the most influential effect on crystal growth [31]. Similar to LTL, we examined more than 30 commercial molecules and identified ZGMs with site specificity for each of the three crystallographic surfaces (Figure 5A). We observed that D-arginine preferentially binds to {101} faces (note that this surface was incorrectly labelled as {302} in the original manuscript). The most effective modifiers of [010] growth were spermine and TBPO. The effect of the former is shown in Figure 5B. The reduction of [010] thickness is of particular importance for mass transport since the preferable channels for sorbate diffusion are oriented in the b-direction. We observed that ZGMs reduce the diffusion path length by nearly an order of magnitude. When comparing the effects of spermine and triethylenetetramine (TETA) – two nearly identical molecules that differ only by the number of carbons separating their amine groups – we observed that the effect of TETA on silicalite-1 growth was negligible compared to spermine (Figure 5C). This outcome further illustrates the subtle nuances of ZGM-crystal molecular recognition.

Aside from their ability to tailor crystal size and habit, zeolite growth modifiers have additional benefits that may

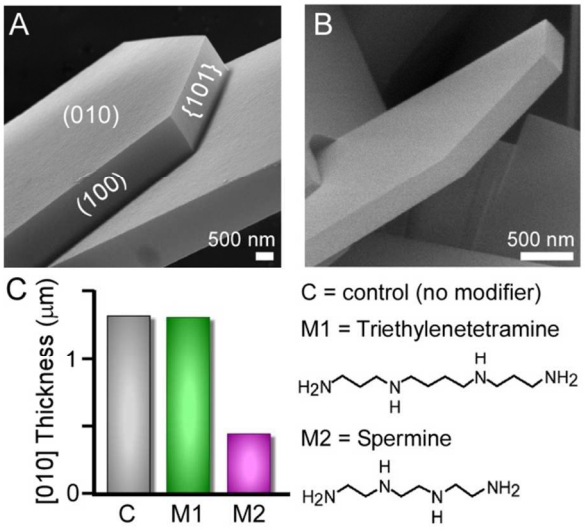

Figure 5. Tailoring the [010] thickness of MFI crystals (silicalite-1). SEM images of crystals prepared (A) in the absence of modifiers (control) and (B) in the presence of 0.5 wt% spermine. (C) Comparison of the [010] dimension for two ZGMs with similar molecular structure. Triethyltetramine (TETA) and spermine differ only by the number of carbons separating their amine groups. The fact that one is an effective ZGM and the other is not highlights the subtle nuances of modifier-crystal molecular recognition.

prove to be useful for catalyst design. For instance, we have shown that ZGMs can selectively tailor the roughness of MFI and LTL crystal surfaces. In aromatization reactions, it has been demonstrated that Pt-LTL crystals with smooth surfaces exhibit longer on-stream lifetime compared to surfaces with roughened exteriors[63]. Similar outcomes for other zeolites could be envisioned; and for reactions where shape selectivity is of little importance, rough exterior surfaces may enhance catalyst activity. For instance, rough surfaces present kinks and defects that may enhance sorbate binding. In addition, the ability to tune surface architecture may prove to be useful in the rational design of zeolite adsorbents.

Multiple Pathways of Zeolite Crystallization

Mechanisms of crystallization are broadly categorized as either classical or non-classical (Figure 6). Surfaces that grow by the former do so by atom or molecule addition. On a molecular level, crystals tend to grow by layered mechanisms. For instance, the AFM 3D height mode image in Figure 6 highlights a silicalite-1 surface comprised of single layers (ca. 0.7nm height) corresponding to a b/2 length of the unit cell. Layers arise from 2D nucleation and grow by solute addition to surface sites (e.g., kink or step sites). Alternatively, layers may emanate from dislocations as growth hillocks that advance across the surface via the direct attachment of building units.

Non-classical pathways have been known to exist since the late 1990s [64], and the list of examples in literature has continued to expand. Non-classical pathways involve precursors, which may be primary particles/clusters or amorphous bulk phases (as illustrated in Figure 6). Nature provides examples of crystals formed through particle-mediated growth, which include iron oxyhydroxide [65, 66], magnetite [67], gypsum [68], noble metals [69, 70], proteins [71], and calcium minerals [72-75]. In some instances precursors are crystalline and undergo oriented attachment to crystal surfaces. In these same systems, misoriented attachment

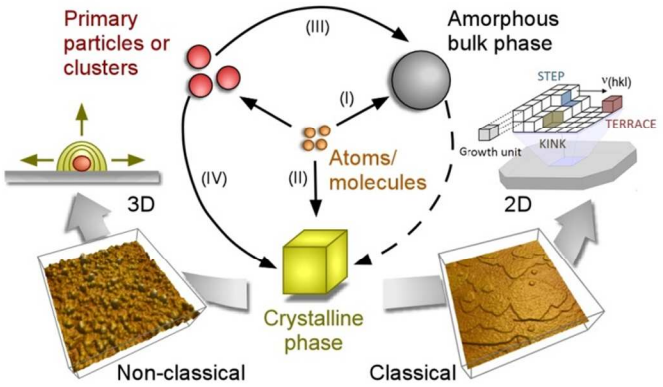

Figure 6. Landscape of mechanistic pathways for zeolite growth by classical and non-classical routes involving the direct addition of atoms/molecules or primary particles, respectively, to growing crystal surfaces. AFM height mode images depict silicalite-1 surface growth by non-classical (left) and classical (right) mechanisms. The schematic was adapted from Baumgartner et al. [67].

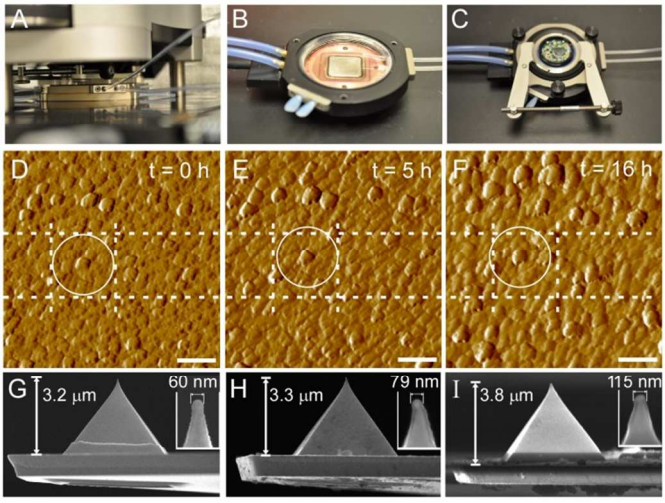

Figure 7. Top row (A – C): AFM instrument. (A) Asylum Research MFP-3D-SA AFM with a retrofitted liquid sample cell. (B) An open sample cell shows the heating Peltier and (C) a closed cell shows the inlet/outlet ports for liquid flow. Middle row (D – F): Lateral drift. Time-resolved AFM continuous imaging of an area (16 hr period) using drift correlation software. Scale bars equal 200 nm. Bottom row (G – I): AFM cantilevers. SEM images reveal a temporal deposition of silica on the AFM tips during *in situ* studies at 80°C, which increases the radius of curvature (insets). Here we highlight (G) a new tip, (H) a tip after a 7 hr equilibration period with periodic imaging, and (I) a tip subjected to 32 hr of continuous imaging following equilibration.

is a possible option that can lead to defects, loss of translational symmetry, or reorientation via Ostwald ripening. There are also examples of amorphous precursors that attach to the crystal surface and undergo post-attachment structural rearrangements to integrate into the underlying topology.

It is postulated that many zeolites grow by non-classical pathways, yet hypotheses in literature are often based on inferences made by virtue of precursor existence in synthesis solutions throughout nucleation and crystal growth. Depending on the selection of synthesis parameters, zeolites can grow from a variety of different media, e.g., aluminosilicate gels, complex fluids comprised of either bulk amorphous aggregates (e.g., worm-like particles[52, 76] or primary particles (1-6 nm)[77], and solids with little solvent[78]. Therefore, it is reasonable to expect that zeolites can grow by any number of possible pathways.

Zeolites crystallize in harsh conditions (i.e., high alkalinity or in HF solutions) and often require high temperature and long synthesis times, which render *in situ* analysis challenging. At macroscopic length scales, growth has been monitored in real time using techniques such as dynamic light scattering (DLS) [79, 80], small-angle X-ray scattering (SAXS)[81, 82], interferometry[83, 84], and others. *Ex situ* techniques such as cryogenic transmission electron microscopy (cryo-TEM) and SEM have proven to be useful for characterizing pre-nuclei shape/structure and crystal size/morphology[85, 86]. Obtaining definitive evidence of crystallization pathway(s), however, requires techniques capable of probing the dynamic events on growing crystal surfaces at near molecular resolution. To this end, our group has pioneered the use of atomic force microscopy (AFM) in solvothermal environments to monitor zeolite surface growth under realistic synthesis conditions.

Addressing the Knowledge Gap in Zeolite Crystal Growth using *In Situ* AFM

Scanning probe microscopy is a useful technique to monitor the growth of crystal surfaces in real time under realistic conditions, yet AFM analyses of zeolites in literature have almost exclusively been *ex situ* studies of crystals extracted from growth solutions. Until recently, *in situ* AFM was restricted to processes that occur at room temperature in short timeframes. The ability to perform similar *in situ* AFM measurements of zeolite growth was long presumed to be an insurmountable task [87]. In particular, there are three aspects that present challenges for AFM measurements of zeolite growth. The first is the need to synthesize crystals with large basal surfaces (e.g., 5 x 5 μm^2 area) to locate and image the crystal. As shown in Figure 1, zeolite crystals are generally not amenable for such studies; they form crystals that are too small (e.g., < 500 nm), exhibit unusual habit, or form aggregates that pose difficulties for mounting samples with the desired surface in the plane of imaging (normal to the AFM tip). A second challenge is lateral drift of the cantilever within the x/y plane, which results in a progressive temporal shift and eventual loss of the initial imaging area. This phenomenon has proven to be less critical when imaging materials that readily crystallize at ambient conditions, such as biogenic crystals [88, 89], zeotypes [90], and metal organic frameworks [91]. High activation energies and concomitant slow rates of zeolite growth necessitate imaging times on the order of hours, which exacerbates lateral drift. A third challenge is the high temperature (> 50 °C) that is necessary to observe dynamic events of surface growth in reasonable timescales. Most conventional AFM instruments are incapable of operating at such high temperature.

In order to perform *in situ* studies, we worked with Asylum Research to design a retrofitted liquid sample cell with features capable of addressing each of the aforementioned challenges. The AFM instrument (Figure 7A) was equipped with a liquid cell built from materials that are resistant to the alkaline solutions used in zeolite synthesis (Figure 7B). The cell was designed with a heating Peltier that regulates the temperature (25 – 300 °C) and inlet/outlet ports for continuous supply of growth solution to the sample (Figure 7C). A critical element of instrument development is the design of drift correlation software that permits imaging for more than 24 hours with less than 200 nm drift in the scanning area (Figure 7, D – F). Imaging in the presence of supersaturated growth solutions results in a progressive deposition of silica on the AFM tip,

which leads to a temporal increase in its radius of curvature (Figure 7, G – I). Changes in tip geometry impact the measured size of surface features; however, systematic calibration of AFM images taken with silica-coated tips revealed less than 2% error in the height and ca. 12% error in the lateral dimensions of surface features [92].

Benchmark tests of the AFM instrument were conducted with silicalite-1 due to its facile synthesis and its traditional use as a prototype for mechanistic studies of zeolite growth. Investigations of silicalite-1 growth have predominantly focused on the identification of primary building units, which have been presumed to be pre-nucleation silica nanoparticles that assemble with remarkably uniform size during tetraethylorthosilicate (TEOS) hydrolysis in aqueous solutions. There is a large body of research over the past two decades that has elucidated the physicochemical properties of precursors, and has provided hypotheses of their putative role(s) in silicalite-1 crystallization. Silica nanoparticles (1–6 nm) [77, 93, 94] initially form metastable core-shells with a disordered siliceous core and a shell of physisorbed OSDA, tetrapropylammonium (TPA).[77] During nucleation a fraction of nanoparticles grow at the expense of others via Ostwald ripening with simultaneous structural transformations, which lead to partially-ordered (non-crystalline) OSDA-silica primary units [82, 85, 95] with unknown microstructure.

Cryo-TEM images have provided evidence that silicalite-1 nucleation occurs by the aggregation and subsequent restructuring of evolved nanoparticles [85, 86]. The observation of ca. 5 nm protrusions on crystal exteriors by *ex situ* TEM [96] and the persistence of precursors in growth solutions throughout silicalite-1 crystallization has led to theories and models postulating that silicalite-1 growth occurs by the direct attachment of precursors [97, 98]. Alternatively, it has been suggested that nanoparticles are metastable nutrient sources that continually supply soluble silica molecules (i.e. monomers and oligomers) as growth units [99-102]. In a recent study, we used *in situ* AFM measurements to show that the mechanism of silicalite-1 growth involves both pathways, thereby bridging hypotheses of classical and non-classical crystallization by molecule and precursor attachment, respectively [92].

Investigations of silicalite-1 surface growth were performed using a supersaturated silica solution with molar composition x SiO_2:y TPAOH:9500 H_2O:4x EtOH (with x = 28 – 48 and y = 3 – 40). AFM images of the (010) face were collected at discrete time points for the first 7 hours of heating at 80 °C. Height mode images revealed the temporal appearance of deposits with dimensions that equal those of silica precursors in solution (Figure 8, A – C). Over the course of the equilibration period, surfaces become laden with nanoparticle deposits. Continuous AFM imaging showed that surface deposits grow in size with the time of heating (Figure 8, D – F). *In situ* AFM studies confirmed that silicalite-1 growth occurs by a combination of precursor attachment and silica molecule addition. Time-resolved images of surface growth captured the birth (3D nucleation), rearrangement, and growth of islands. Prior studies have concluded that precursors are non-crystalline [95, 103]; therefore, the complete integration of precursors into the underlying MFI topology necessitates some degree of post-attachment restructuring. Indeed, AFM snapshots of surface growth reveal the disappearance of features and the reduction of island height attributed to the structural rearrangement of precursors (i.e., disorder-to-order transition).

AFM analysis of silicalite-1 generated the first *in situ* evidence of zeolite surface growth. From these results we identified two concerted pathways of crystallization involving 3-dimensional nucleation and growth of islands, which stands in stark contrast to the layer-by-layer mechanism (see Figure 6). The fact that classical and non-classical pathways are simultaneously at play alludes to a more widespread mechanism of zeolite growth; however, it should be noted that the starting solutions for zeolite synthesis can be vastly different from those encountered for silicalite-1. The latter is most commonly prepared with clear solutions derived from TEOS, yet the majority of zeolites are synthesized from alternative silica sources, such as colloidal or fumed silica. Moreover, precursors in these complex fluids tend to be amorphous bulk phases with sizes much larger than the silica nanoparticles in silicalite-1 syntheses. There have been many theories postulated for the disorder-to-order transition of such precursors to zeolite crystals; and it is more often the case that detailed mechanisms are gleaned from *ex situ* data without direct evidence to support the individual steps postulated for nucleation and crystal growth. The advent of *in situ* techniques, such as AFM, open avenues to explore zeolite growth at near molecular length scales. Future research in this area would benefit from a more open mind set that allows for multiple pathways of growth, recognizing that the mechanism may be different from one zeolite to the next, or even for the same zeolite prepared by different techniques. The complexity of zeolite crystallization renders the identification of mechanisms a daunting task, but advancements in this area of research can benefit catalyst design. Specifically, the ability to *a priori* control physicochemical properties such as size and shape of zeolites requires fundamental knowledge of their growth if we are to selectively tune their anisotropic rates of growth.

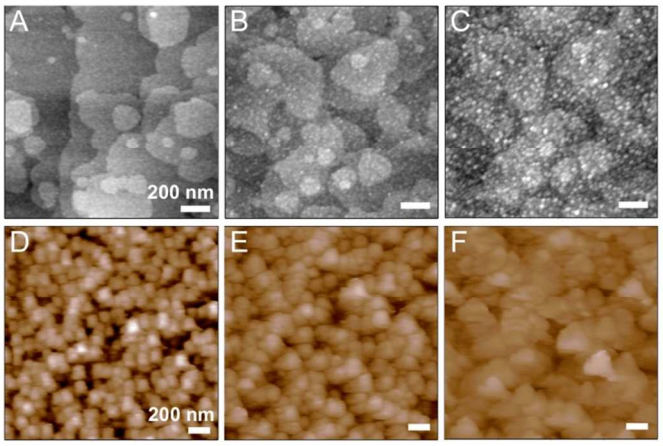

Figure 8. Time-resolved AFM images of silicalite-1 (010) surface growth in supersaturated silica solutions at 80 ºC. Periodic imaging during the first 7 hours of heating (equilibration period) reveals the progressive deposition of precursors on the crystal surface: (A) 0 hr, (B) 3.5 hr, and (C) 7 hr. Continuous imaging of the surface after the 7 hr equilibration period at 80 ºC reveals the 3-dimensional growth of precursor deposits: (D) 0 hr, (E) 5 hr, and (F) 10 hr.

Conclusions

The performance of zeolite catalysts can be markedly enhanced through rational design; however, the complexity of zeolite crystallization necessitates concerted efforts in both fundamental and applied research to optimize catalyst synthesis. To this end, we have discussed three areas of research that focus on distinct, yet highly synergistic, ways of

controlling crystal growth and the physicochemical properties of zeolite catalysts. The ability to utilize multiple approaches, such as OSDA-free synthesis and ZGM design, offers a promising route to expand the list of available framework types for industrial catalysis, as well as improve catalysts for a variety of applications. A combination of these approaches with the innovative *in situ* AFM technique affords new opportunities to explore the mechanisms of crystallization, and guide pathways in crystal engineering that utilize economical, versatile, and predictive methods to foster breakthroughs in zeolite synthesis that are of commercial relevance.

Acknowledgements

This work was financially supported by NSF (CAREER 1151098), ACS PRF (Award 52422-DNI5), the Norman Hackerman Advanced Research Program (Award 003652-0024-2011), and The Welch Foundation (Award E-1794).

Notes and references

[a] University of Houston, Department of Chemical and Biomolecular Engineering, 4800 Calhoun Rd., Houston, TX 77204 USA.

* Corresponding Author: jrimer@central.uh.edu

† Electronic Supplementary Information (ESI) available: Experimental methods; characterization techniques; list of OSDA-free synthesis compositions; list of ZGMs for MOR synthesis; and XRD spectra for MER and MOR zeolites. See DOI: 10.1039/b000000x/

1. C. L. Williams, C. C. Chang, P. Do, N. Nikbin, S. Caratzoulas, D. G. Vlachos, R. F. Lobo, W. Fan and P. J. Dauenhauer, *Acs Catalysis*, 2012, 2, 935-939.
2. J. H. Kwak, R. G. Tonkyn, D. H. Kim, J. Szanyi and C. H. F. Peden, *Journal of Catalysis*, 2010, 275, 187-190.
3. M. Colombo, I. Nova and E. Tronconi, *Catal. Today*, 2010, 151, 223-230.
4. D. W. Fickel, J. M. Fedeyko and R. F. Lobo, *Journal of Physical Chemistry C*, 2010, 114, 1633-1640.
5. U. Olsbye, S. Svelle, M. Bjorgen, P. Beato, T. V. Janssens, F. Joensen, S. Bordiga and K. P. Lillerud, *Angew Chem Int Ed Engl*, 2012, 51, 5810-5831.
6. S. Ilias and A. Bhan, *Acs Catalysis*, 2013, 3, 18-31.
7. J. J. Spivey and G. Hutchings, *Chemical Society Reviews*, 2014, 43, 792-803.
8. International Zeolite Association, www.iza-online.org.
9. M. E. Davis, *Chem. Mat.*, 2014, 26, 239-245.
10. A. Corma, F. Rey, J. Rius, M. J. Sabater and S. Valencia, *Nature*, 2004, 431, 287-290.
11. G. J. Yang, Y. X. Wei, S. T. Xu, J. R. Chen, J. Z. Li, Z. M. Li, J. H. Yu and R. R. Xu, *Journal of Physical Chemistry C*, 2013, 117, 8214-8222.
12. C. Jo, J. Jung, H. S. Shin, J. Kim and R. Ryoo, *Angewandte Chemie-International Edition*, 2013, 52, 10014-10017.
13. M. Choi, K. Na, J. Kim, Y. Sakamoto, O. Terasaki and R. Ryoo, *Nature*, 2009, 461, 246-U120.
14. J. L. Sun, C. Bonneau, A. Cantin, A. Corma, M. J. Diaz-Cabanas, M. Moliner, D. L. Zhang, M. R. Li and X. D. Zou, *Nature*, 2009, 458, 1154-U1190.
15. V. P. Valtchev and L. Tosheva, *Chemical Reviews*, 2013, DOI: 10.1021/cr300439k.
16. G. Majano, A. Darwiche, S. Mintova and V. Valtchev, *Industrial & Engineering Chemistry Research*, 2009, 48, 7084-7091.
17. P. Sharma, P. Rajaram and R. Tomar, *Journal of Colloid and Interface Science*, 2008, 325, 547-557.
18. X. Zhang, D. Liu, D. Xu, S. Asahina, K. A. Cychosz, K. V. Agrawal, Y. Al Wahedi, A. Bhan, S. Al Hashimi, O. Terasaki, M. Thommes and M. Tsapatsis, *Science*, 2012, 336, 1684-1687.
19. M. Tsapatsis, *Science*, 2011, 334, 767-768.
20. A. Corma, V. Fornes, S. B. Pergher, T. L. M. Maesen and J. G. Buglass, *Nature*, 1998, 396, 353-356.
21. K. Varoon, X. Y. Zhang, B. Elyassi, D. D. Brewer, M. Gettel, S. Kumar, J. A. Lee, S. Maheshwari, A. Mittal, C. Y. Sung, M. Cococcioni, L. F. Francis, A. V. McCormick, K. A. Mkhoyan and M. Tsapatsis, *Science*, 2011, 333, 72-75.
22. I. Ogino, M. M. Nigra, S. J. Hwang, J. M. Ha, T. Rea, S. I. Zones and A. Katz, *J. Am. Chem. Soc.*, 2011, 133, 3288-3291.
23. W. Fan, M. A. Snyder, S. Kumar, P. S. Lee, W. C. Yoo, A. V. McCormick, R. L. Penn, A. Stein and M. Tsapatsis, *Nature Materials*, 2008, 7, 984-991.
24. Z. Wang, P. Dornath, C.-C. Chang, H. Chen and W. Fan, *Microporous Mesoporous Mat.*, 2013, 181, 8-16.
25. Y. Liu, X. Z. Zhou, X. M. Pang, Y. Y. Jin, X. J. Meng, X. M. Zheng, X. H. Gao and F. S. Xiao, *ChemCatChem*, 2013, 5, 1517-1523.
26. S. R. Venna and M. A. Carreon, *J. Phys. Chem. B*, 2008, 112, 16261-16265.
27. Z. C. Shan, H. Wang, X. J. Meng, S. Y. Liu, L. A. Wang, C. Y. Wang, F. Li, J. P. Lewis and F. S. Xiao, *Chem. Commun.*, 2011, 47, 1048-1050.
28. C. S. Carr and D. F. Shantz, *Chem. Mat.*, 2005, 17, 6192-6197.
29. S. Lee and D. F. Shantz, *Chem. Commun.*, 2004, DOI: 10.1039/b315646j, 680-681.
30. A. I. Lupulescu, M. Kumar and J. D. Rimer, *J. Am. Chem. Soc.*, 2013, 135, 6608-6617.
31. A. I. Lupulescu and J. D. Rimer, *Angewandte Chemie-International Edition*, 2012, 51, 3345-3349.
32. M. D. Oleksiak and J. D. Rimer, *Reviews in Chemical Engineering*, 2014, 30, 1-49.
33. V. J. Inglezakis and A. A. Zorpas, *Handbook of Natural Zeolites*, Bentham Science Publishers, 2012.
34. A. Navrotsky, O. Trofymluk and A. A. Levchenko, *Chemical Reviews*, 2009, 109, 3885-3902.
35. M. Maldonado, M. D. Oleksiak, S. Chinta and J. D. Rimer, *J. Am. Chem. Soc.*, 2013, 135, 2641-2652.
36. M. T. Melchior, D. E. W. Vaughan and A. J. Jacobson, *J. Am. Chem. Soc.*, 1982, 104, 4859-4864.
37. M. Moliner, Y. Roman-Leshkov and M. E. Davis, *Proceedings of the National Academy of Sciences of the United States of America*, 2010, 107, 6164-6168.
38. E. A. Eilertsen, B. Arstad, S. Svelle and K. P. Lillerud, *Microporous Mesoporous Mat.*, 2012, 153, 94-99.
39. *U.S. Pat.,* 4,299,686, 1981.
40. Y. Kamimura, K. Iyoki, S. P. Elangovan, K. Itabashi, A. Shimojima and T. Okubo, *Microporous Mesoporous Mat.*, 2012, 163, 282-290.
41. Y. Kamimura, S. Tanahashi, K. Itabashi, A. Sugawara, T. Wakihara, A. Shimojima and T. Okubo, *Journal of Physical Chemistry C*, 2011, 115, 744-750.
42. K. Itabashi, Y. Kamimura, K. Iyoki, A. Shimojima and T. Okubo, *J. Am. Chem. Soc.*, 2012, 134, 11542-11549.
43. B. Xie, J. W. Song, L. M. Ren, Y. Y. Ji, J. X. Li and F. S. Xiao, *Chem. Mat.*, 2008, 20, 4533-4535.
44. B. Xie, H. Y. Zhang, C. G. Yang, S. Y. Liu, L. M. Ren, L. Zhang, X. J. Meng, B. Yilmaz, U. Muller and F. S. Xiao, *Chem. Commun.*, 2011, 47, 3945-3947.
45. Y. Q. Wang, X. Wang, Q. M. Wu, X. J. Meng, Y. Y. Jin, X. Z. Zhou and F. S. Xiao, *Catal. Today*, 2014, 226, 103-108.

46. Q. M. Wu, X. Wang, X. J. Meng, C. G. Yang, Y. Liu, Y. Y. Jin, Q. Yang and F. S. Xiao, *Microporous Mesoporous Mat.*, 2014, 186, 106-112.
47. Z. F. Wu, J. W. Song, Y. Y. Ji, L. M. Ren and F. S. Xiao, *Chem. Mat.*, 2008, 20, 357-359.
48. C. G. Yang, L. M. Ren, H. Y. Zhang, L. F. Zhu, L. Wang, X. J. Meng and F. S. Xiao, *J. Mater. Chem.*, 2012, 22, 12238-12245.
49. L. Van Tendeloo, E. Gobechiya, E. Breynaert, J. A. Martens and C. E. A. Kirschhock, *Chem. Commun.*, 2013, 49, 11737-11739.
50. M. Moliner, C. Franch, E. Palomares, M. Grill and A. Corma, *Chem. Commun.*, 2012, 48, 8264-8266.
51. S. Goel, Z. J. Wu, S. I. Zones and E. Iglesia, *J. Am. Chem. Soc.*, 2012, 134, 17688-17695.
52. O. Larlus and V. P. Valtchev, *Chem. Mat.*, 2004, 16, 3381-3389.
53. A. Z. Ruiz, D. Bruhwiler, T. Ban and G. Calzaferri, *Monatshefte Fur Chemie*, 2005, 136, 77-89.
54. Y. J. Lee, J. S. Lee and K. B. Yoon, *Microporous Mesoporous Mat.*, 2005, 80, 237-246.
55. L. Zhang, A. N. C. van Laak, P. E. de Jongh and K. P. de Jong, *Microporous Mesoporous Mat.*, 2009, 126, 115-124.
56. V. Valtchev and L. Tosheva, *Chemical Reviews*, 2013, 113, 6734-6760.
57. M. Tsapatsis, M. Lovallo, T. Okubo, M. E. Davis and M. Sadakata, *Chem. Mat.*, 1995, 7, 1734-1741.
58. S. I. Zones, *Microporous Mesoporous Mat.*, 2011, 144, 1-8.
59. J. P. Sizemore and M. F. Doherty, *Crystal Growth & Design*, 2009, 9, 2637-2645.
60. M. B. Dickerson, K. H. Sandhage and R. R. Naik, *Chemical Reviews*, 2008, 108, 4935-4978.
61. W.-C. Huang, L.-M. Lyu, Y.-C. Yang and M. H. Huang, *J. Am. Chem. Soc.*, 2011, 134, 1261-1267.
62. C.-Y. Chiu, H. Wu, Z. Yao, F. Zhou, H. Zhang, V. Ozolins and Y. Huang, *J. Am. Chem. Soc.*, 2013, 135, 15489-15500.
63. S. Trakarnroek, S. Jongpatiwut, T. Rirksomboon, S. Osuwan and D. E. Resasco, *Applied Catalysis a-General*, 2006, 313, 189-199.
64. P. Dandekar and M. F. Doherty, *Science*, 2014, 344, 705-706.
65. J. F. Banfield, S. A. Welch, H. Z. Zhang, T. T. Ebert and R. L. Penn, *Science*, 2000, 289, 751-754.
66. D. S. Li, M. H. Nielsen, J. R. I. Lee, C. Frandsen, J. F. Banfield and J. J. De Yoreo, *Science*, 2012, 336, 1014-1018.
67. J. Baumgartner, A. Dey, P. H. H. Bomans, C. Le Coadou, P. Fratzl, N. Sommerdijk and D. Faivre, *Nature Materials*, 2013, 12, 310-314.
68. A. E. S. Van Driessche, L. G. Benning, J. D. Rodriguez-Blanco, M. Ossorio, P. Bots and J. M. Garcia-Ruiz, *Science*, 2012, 336, 69-72.
69. H. G. Liao, L. K. Cui, S. Whitelam and H. M. Zheng, *Science*, 2012, 336, 1011-1014.
70. H. M. Zheng, R. K. Smith, Y. W. Jun, C. Kisielowski, U. Dahmen and A. P. Alivisatos, *Science*, 2009, 324, 1309-1312.
71. S. T. Yau and P. G. Vekilov, *J. Am. Chem. Soc.*, 2001, 123, 1080-1089.
72. D. Gebauer, A. Volkel and H. Colfen, *Science*, 2008, 322, 1819-1822.
73. W. Habraken, J. H. Tao, L. J. Brylka, H. Friedrich, L. Bertinetti, A. S. Schenk, A. Verch, V. Dmitrovic, P. H. H. Bomans, P. M. Frederik, J. Laven, P. van der Schoot, B. Aichmayer, G. de With, J. J. DeYoreo and N. Sommerdijk, *Nature Communications*, 2013, 4.
74. E. M. Pouget, P. H. H. Bomans, J. Goos, P. M. Frederik, G. de With and N. Sommerdijk, *Science*, 2009, 323, 1455-1458.
75. A. F. Wallace, L. O. Hedges, A. Fernandez-Martinez, P. Raiteri, J. D. Gale, G. A. Waychunas, S. Whitelam, J. F. Banfield and J. J. De Yoreo, *Science*, 2013, 341, 885-889.
76. N. Ren, B. Subotić, J. Bronić, Y. Tang, M. D. Sikirić, T. Mišić, V. Svetličić, S. Bosnar and T. A. Jelić, *Chem. Mat.*, 2012, 24, 1726-1737.
77. J. M. Fedeyko, J. D. Rimer, R. F. Lobo and D. G. Vlachos, *J. Phys. Chem. B*, 2004, 108, 12271-12275.
78. X. J. Meng and F. S. Xiao, *Chemical Reviews*, 2014, 114, 1522-1544.
79. B. J. Schoeman, *Zeolites*, 1997, 18, 97-105.
80. J. N. Watson, L. E. Iton, R. I. Keir, J. C. Thomas, T. L. Dowling and J. W. White, *J. Phys. Chem. B*, 1997, 101, 10094-10104.
81. P. de Moor, T. P. M. Beelen, R. A. van Santen, K. Tsuji and M. E. Davis, *Chem. Mat.*, 1999, 11, 36-43.
82. J. D. Rimer, D. G. Vlachos and R. F. Lobo, *J. Phys. Chem. B*, 2005, 109, 12762-12771.
83. A. Iwasaki, M. Hirata, I. Kudo and T. Sano, *Zeolites*, 1996, 16, 35-41.
84. B. Holme, P. Cubillas, J. H. Cavka, B. Slater, M. W. Anderson and D. Akporiaye, *Crystal Growth & Design*, 2010, 10, 2824-2828.
85. T. M. Davis, T. O. Drews, H. Ramanan, C. He, J. S. Dong, H. Schnablegger, M. A. Katsoulakis, E. Kokkoli, A. V. McCormick, R. L. Penn and M. Tsapatsis, *Nature Materials*, 2006, 5, 400-408.
86. S. Kumar, Z. P. Wang, R. L. Penn and M. Tsapatsis, *J. Am. Chem. Soc.*, 2008, 130, 17284-+.
87. L. I. Meza, M. W. Anderson, J. R. Agger, C. S. Cundy, C. B. Chong and R. J. Plaisted, *J. Am. Chem. Soc.*, 2007, 129, 15192-15201.
88. J. D. Rimer, Z. An, Z. Zhu, M. H. Lee, D. S. Goldfarb, J. A. Wesson and M. D. Ward, *Science*, 2010, 330, 337-341.
89. C. A. Orme, A. Noy, A. Wierzbicki, M. T. McBride, M. Grantham, H. H. Teng, P. M. Dove and J. J. DeYoreo, *Nature*, 2001, 411, 775-779.
90. M. A. Holden, P. Cubillas, M. P. Attfield, J. T. Gebbie and M. W. Anderson, *J. Am. Chem. Soc.*, 2012, 134, 13066-13073.
91. P. Cubillas, M. W. Anderson and M. P. Attfield, *Chemistry-a European Journal*, 2013, 19, 8236-8243.
92. A. I. Lupulescu and J. D. Rimer, *Science*, 2014, 344, 729-732.
93. P. de Moor, T. P. M. Beelen, B. U. Komanschek, O. Diat and R. A. van Santen, *J. Phys. Chem. B*, 1997, 101, 11077-11086.
94. J. N. Watson, L. E. Iton and J. W. White, *Chem. Commun.*, 1996, 2767-2768.
95. J. D. Rimer, O. Trofymluk, A. Navrotsky, R. F. Lobo and D. G. Vlachos, *Chem. Mat.*, 2007, 19, 4189-4197.
96. S. Kumar, T. M. Davis, H. Ramanan, R. L. Penn and M. Tsapatsis, *The Journal of Physical Chemistry B*, 2007, 111, 3398-3403.
97. T. O. Drews, M. A. Katsoulakis and M. Tsapatsis, *J. Phys. Chem. B*, 2005, 109, 23879-23887.
98. V. Nikolakis, E. Kokkoli, M. Tirrell, M. Tsapatsis and D. G. Vlachos, *Chem. Mat.*, 2000, 12, 845-853.
99. B. J. Schoeman, *Microporous Mesoporous Mat.*, 1998, 22, 9-22.
100. S. L. Burkett and M. E. Davis, *Chem. Mat.*, 1995, 7, 920-928.
101. S. Kumar, R. L. Penn and M. Tsapatsis, *Microporous Mesoporous Mat.*, 2011, 144, 74-81.
102. A. Aerts, L. R. A. Follens, E. Biermans, S. Bals, G. Van Tendeloo, B. Loppinet, C. E. A. Kirschhock and J. A. Martens, *Physical Chemistry Chemical Physics*, 2011, 13, 4318-4325.
103. C. T. G. Knight, J. P. Wang and S. D. Kinrade, *Physical Chemistry Chemical Physics*, 2006, 8, 3099-3103.

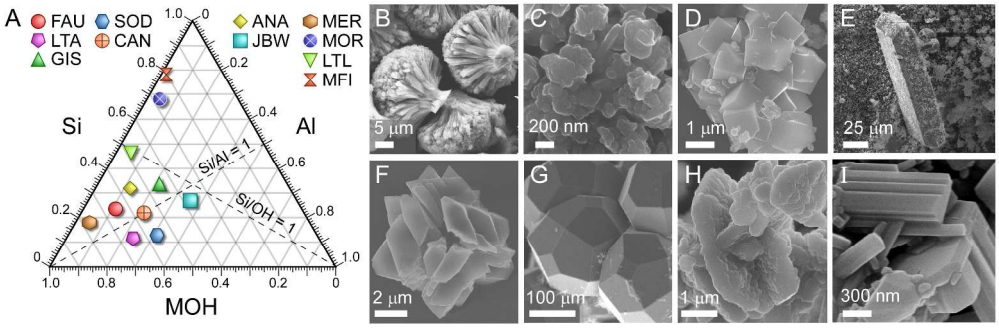

Figure 1. (A) Kinetic phase diagram highlighting representative molar fractions of zeolites prepared with alkali metals (M+ = Na+ or K+) and without OSDAs (Table S1 in SI lists specific growth conditions). Scanning electron micrographs of the zeolite crystals (B) K-MER, (C) Na-FAU, (D) Na-LTA, (E) Na-JBW, (F) Na-GIS, (G) Na-ANA, (H) Na-SOD, and (I) Na-CAN. Images of K-LTL and Na-MOR are in Figures 2 and 3.
436x145mm (190 x 190 DPI)

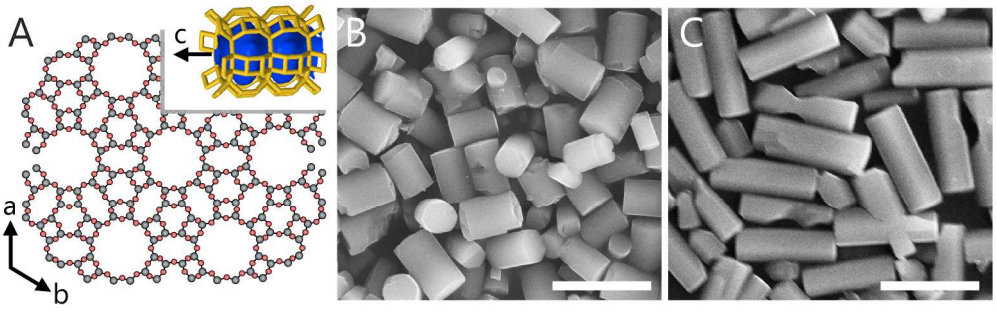

Figure 2. LTL crystallization. (A) LTL is a hexagonal structure with a P6/mmm space group (a = 1.81, b = 1.81, c = 0.76 nm; α = β = 90°, γ = 120°; _V = 36.0 cm3/mol). (B) Scanning electron micrographs of K-LTL prepared at a molar ratio 10 KOH:z H2O (z = 505). LTL crystallization is sensitive to water content. (C) SEM image of crystals prepared with increased water content, z = 603. Scale bars equal 5 microns.
275x86mm (240 x 240 DPI)

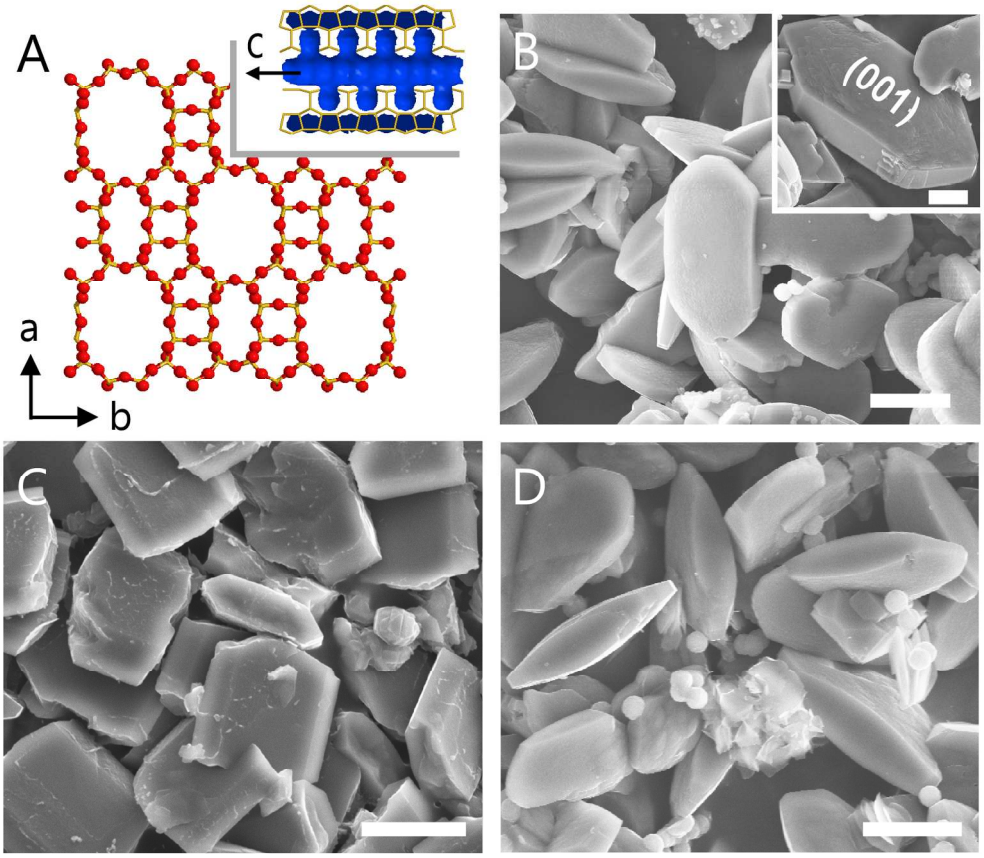

Figure 3. MOR crystallization. (A) MOR is an orthorhombic structure with a Cmcm space group (a = 1.83, b = 2.05, c = 0.75 nm; $\alpha = \beta = \gamma = 90°$; _V = 35.4 cm3/mol). (B) Na-MOR crystals are hexagonal platelets with (001) basal faces (inset). Scanning electron micrographs of crystals synthesized in the presence of (C) cyclohexane-1,4-diol and (D) tributylphosphine oxide (TBPO). These ZGMs result in an elongation of crystal dimension in the c-direction and a narrowing of the (001) surface area, respectively. Scale bars equal 10 microns.
303x267mm (160 x 160 DPI)

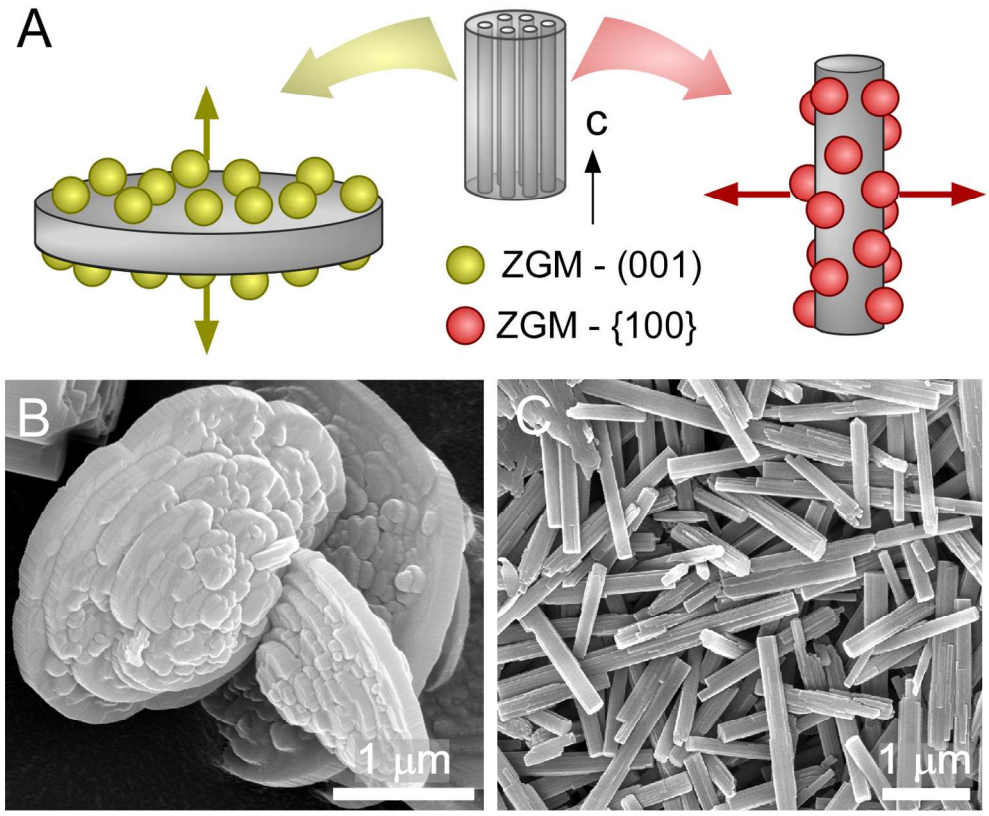

Figure 4. Effects of growth modifiers on LTL crystal habit. (A) Illustration of modifier-crystal interactions on the (001) and {100} surfaces, producing (B) low aspect ratio discs and (C) high aspect ratio rod-like crystals, respectively. LTL crystals in the SEM images were prepared with the following modifiers: (B) 1,2,3-hexanetriol (10 wt%) and (C) PDDAC (2 wt%).
172x144mm (240 x 240 DPI)

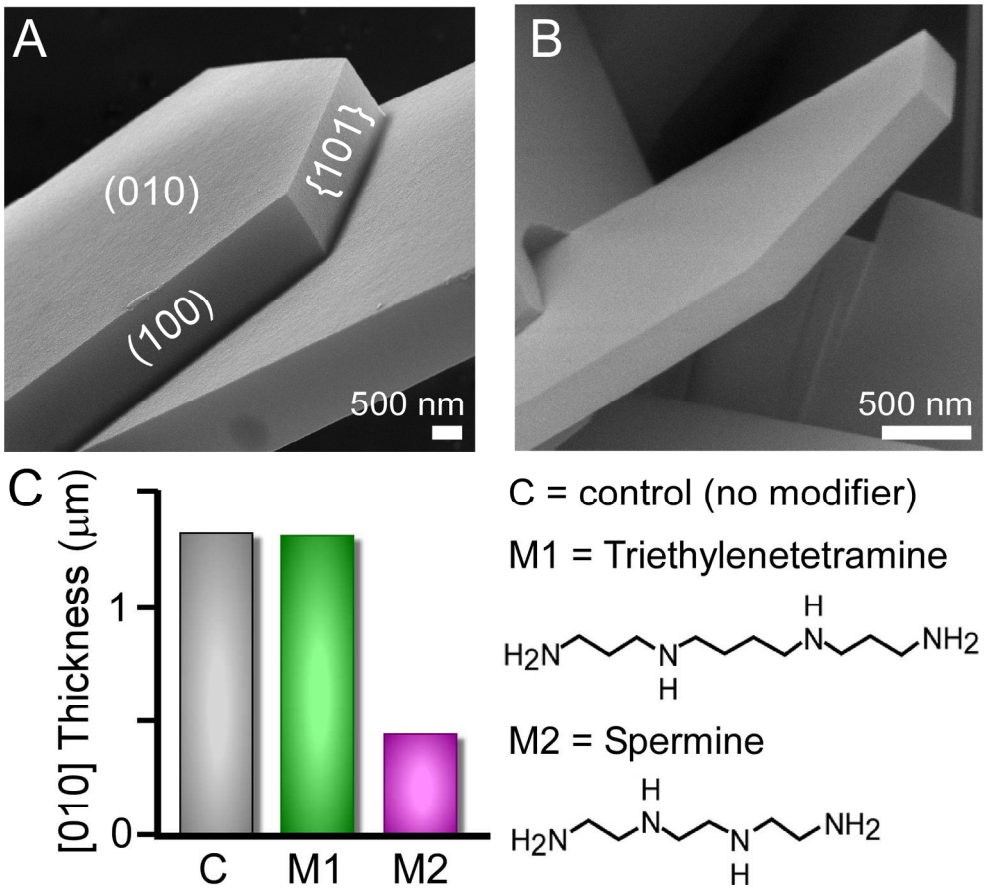

Figure 5. Tailoring the [010] thickness of MFI crystals (silicalite-1). SEM images of crystals prepared (A) in the absence of modifiers (control) and (B) in the presence of 0.5 wt% spermine. (C) Comparison of the [010] dimension for two ZGMs with similar molecular structure. Triethyltetramine (TETA) and spermine differ only by the number of carbons separating their amine groups. The fact that one is an effective ZGM and the other is not highlights the subtle nuances of modifier-crystal molecular recognition.
205x187mm (240 x 240 DPI)

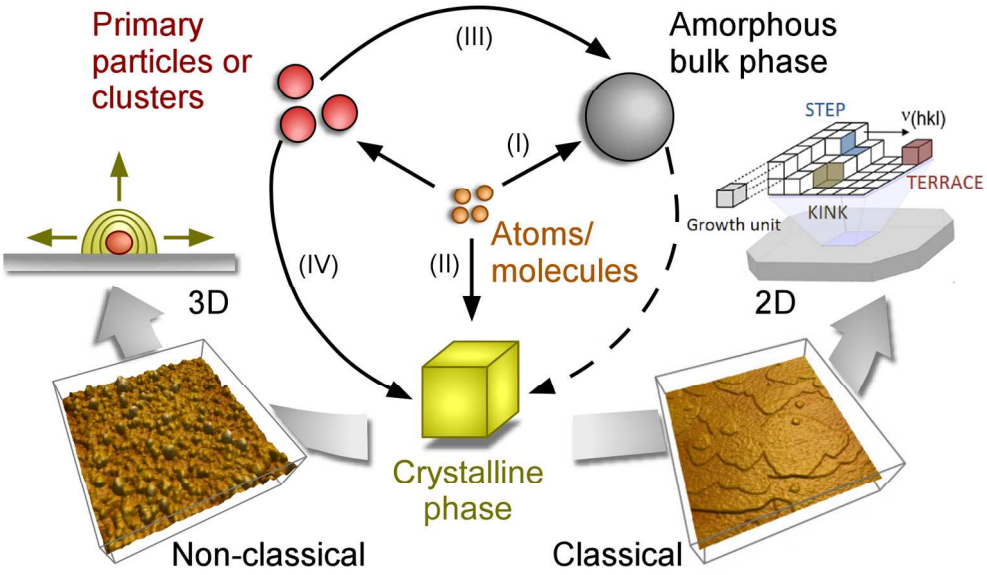

Figure 6. Landscape of mechanistic pathways for zeolite growth by classical and non-classical routes involving the direct addition of atoms/molecules or primary particles, respectively, to growing crystal surfaces. AFM height mode images depict silicalite-1 surface growth by non-classical (left) and classical (right) mechanisms. The schematic was adapted from Baumgartner et al. (ref 56).
194x114mm (250 x 250 DPI)

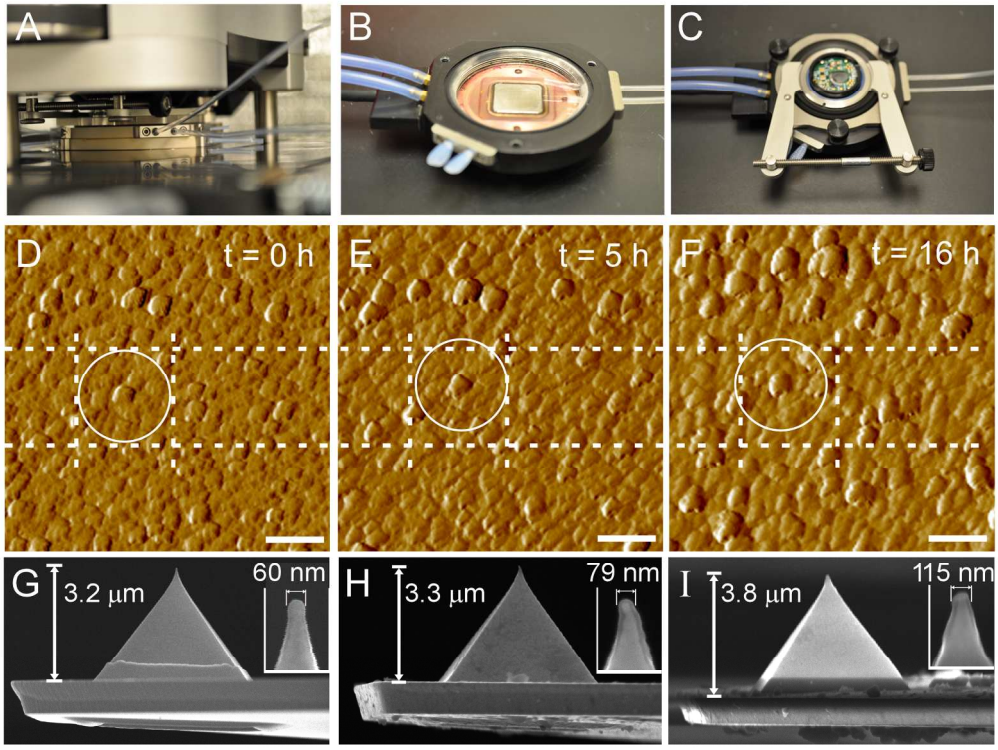

Figure 7. Top row (A – C): AFM instrument. (A) Asylum Research MFP-3D-SA AFM with a retrofitted liquid sample cell. (B) An open sample cell shows the heating Peltier and (C) a closed cell shows the inlet/outlet ports for liquid flow. Middle row (D – F): Lateral drift. Time-resolved AFM continuous imaging of an area (16 hr period) using drift correlation software. Scale bars equal 200 nm. Bottom row (G – I): AFM cantilevers. SEM images reveal a temporal deposition of silica on the AFM tips during in situ studies at 80°C, which increases the radius of curvature (insets). Here we highlight (G) a new tip, (H) a tip after a 7 hr equilibration period with periodic imaging, and (I) a tip subjected to 32 hr of continuous imaging following equilibration.
336x253mm (170 x 170 DPI)

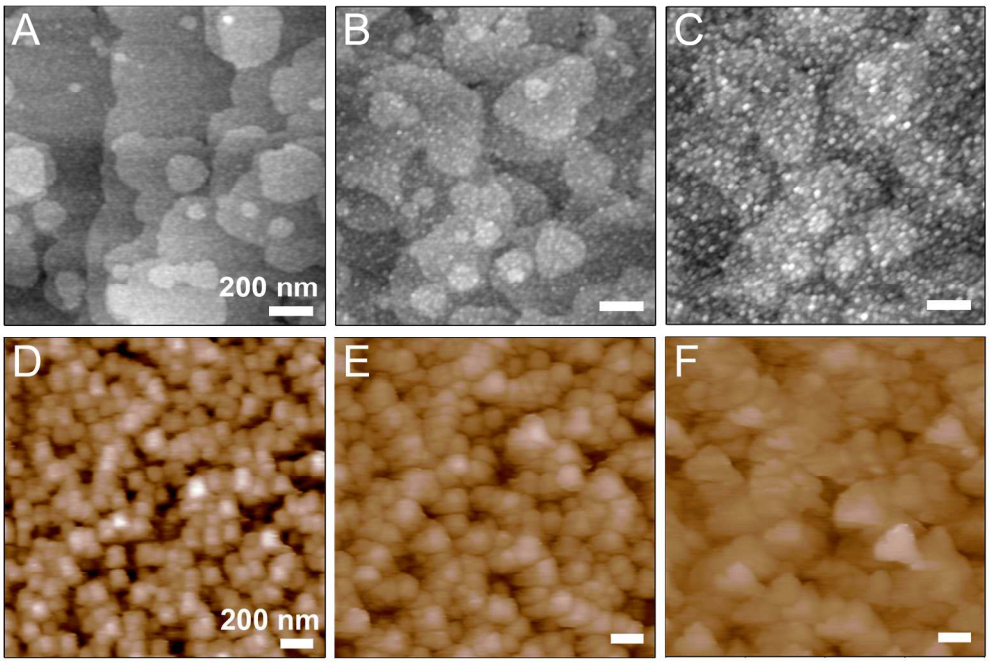

Figure 8. Time-resolved AFM images of silicalite-1 (010) surface growth in supersaturated silica solutions at 80 ºC. Periodic imaging during the first 7 hours of heating (equilibration period) reveals the progressive deposition of precursors on the crystal surface: (A) 0 hr, (B) 3.5 hr, and (C) 7 hr. Continuous imaging of the surface after the 7 hr equilibration period at 80 ºC reveals the 3-dimensional growth of precursor deposits: (D) 0 hr, (E) 5 hr, and (F) 10 hr.
292x196mm (190 x 190 DPI)